Investigation of thermal energy potential, pyroelectric, and electrocaloric performance of $Ba_{0.7}Ca_{0.3}TiO_3$ ceramic

A. Ray[1,2] · B. Nayak[2,3] · P. Elorika[2,3] · R. Barman[1] · A. Sharmistha[2,3] · T. Badapanda[1] · S. Anwar[2,3]

Abstract

In the current work, the structural, dielectric, and electrocaloric performance of $Ba_{0.7}Ca_{0.3}TiO_3$ ceramic synthesized by solid-state reaction route is presented. The structural analysis was examined by X-ray diffraction and Rietveld refinement, which confirms the existence of a combined phase of tetragonal structure with P4mm symmetry and orthorhombic structure with Amm2 symmetry. The scanning electron micrograph shows well-defined and pore-free grains. The temperature-dependent dielectric performance shows diffuse phase transition behavior. The temperature-dependent ferroelectric hysteresis behavior was examined under the application of various amplitudes of an applied electric field. The energy storage density, energy loss density, and energy storage efficiency of the composition at different temperature were calculated using the standard formula. The thermal energy potential has been calculated by employing the Olsen cycle. Also, pyroelectric figures of merit (FOMs) for voltage responsivity (F_v), current responsivity (F_i), energy harvesting (F_e), new energy harvesting (F_e^*), and detective (F_d) were calculated. Adiabatic temperature change, isothermal entropy change, and electrocaloric strength are evaluated using an indirect technique based on the thermodynamic Maxwell's relation.

Keywords Lead-free ceramic · Dielectric · Ferroelectric · Olsen cycle · Electrocaloric effect · Pyroelectric coefficient

1 Introduction

The demand for cooling and air-conditioning equipment is driving up global power consumption. The issues of environmental concern and poor cooling efficiency plague the cooling technology that is now in use, such as semiconductor refrigeration and vapor compression. As a result, researchers are putting a lot of effort into creating new eco-friendly refrigeration technologies. An inventive and promising method to realize high efficiency and environment friendly cooling in the future is provided by the thermal change in ferroic materials that is caused by external stimuli, such as

magnetic, electric, pressure, and mechanical fields, which correspond to the magnetocaloric (MC), electrocaloric (EC), barocaloric (BC), and mechanocaloric (mC) effects, respectively [1–9]. Compact device designs, lightweight, and relatively easy creation and control of electric fields are the appealing characteristics of EC cooling as compared to the MC, BC, and mC effects [10, 11]. A cutting-edge alternative technology known as the electrocaloric effect (ECE) changes the entropy (ΔS) and temperature (ΔT) of polar materials in the presence of an external electric field (E).

The EC effect is a relatively recent and challenging research topic in the study of ferroelectric materials. Recently, the use of ferroelectric materials for EC refrigeration has attracted a lot of attention for solid-state cooling applications. Because of the relative mobility of the ions in the structure under the applied electric field, the change in entropy (S), which is controlled by the change of ferroelectric dipolar, is the basic mechanism underlying the ECE in ferroelectric materials. Among lead-free ceramics, BT is one of the potential competitors in this market. The three distinct phase transitions that are evident are the tetragonal-cubic phase transition ($T_C = 120$ °C), the orthorhombic–tetragonal phase transition ($T_{O-T} = 0$ °C),

✉ T. Badapanda
badapanda.tanmaya@gmail.com

✉ S. Anwar
shahidanwr@gmail.com; shahid@immt.res.in

1 Department of Physics, C.V. Raman Global University, Bhubaneswar 752054, India

2 CSIR-Institute of Minerals and Materials Technology, Bhubaneswar 751013, India

3 Academy of Scientific and Innovative Research (AcSIR), Ghaziabad, Uttar Pradesh 201002, India

and the rhombohedral–orthorhombic phase transition ($T_{R-O} = 90$ °C) [12, 13]. It exhibits a low dielectric constant, and moderate energy storage capabilities. Therefore, several site engineering procedures including the substitution of different dopants in the Ba site and/or Ti site have been used to improve these features [14–16]. The discovery of morphotropic phase boundary (MPB) and multi-phase coexistence, which can considerably improve the characteristics of BT-based ceramics, was the most significant advancement in BT-based systems over the decades [17, 18]. The extension process and polarization rotation are made simpler by the low energy barriers in the MPB area, which improves the ferroelectric and piezoelectric capabilities.

Ca is discovered to be one of the most suitable dopants for enhancing the dielectric performance of the BT-based system. Due to the larger ionic radius of the barium ion in the BTO ceramic, the addition of the Ca^{2+} ion produces several impacts on the compound structure. This could enlarge the octahedral site and demonstrate the removal of the Ti^{4+} ion from its original location. Much attention is being drawn to the use of Ca^{2+} instead of Ba^{2+} in the BT lattice as a superior ceramic capacitor material that improves the temperature dependence and dependability of the dielectric characteristic of BT-based materials for electronic applications. The Curie temperature is barely affected by the partial replacement of Ca^{2+} for Ba^{2+}; however, the temperature at which the tetragonal to orthorhombic phase transition occurs is significantly lowered, improving the thermal stability of the tetragonal phase. Additionally, $Ba_{0.7}Ca_{0.3}TiO_3$ (BCT) exhibits an intriguing biphasic presence of tetragonal and orthorhombic crystal forms in the $BaTiO_3$-$CaTiO_3$ binary phase diagram, giving the materials strong dielectric permittivity and good piezoelectric characteristics [19]. The analysis of the structural, dielectric, and ferroelectric properties of BCT ceramics has been covered in several studies [20–26]. However, there are not many reports available on the thermal energy storage and electrocaloric performance of the BCT ceramic. Here, we report temperature-dependent hysteresis at various electric fields as well as structural, microstructural, and dielectric behavior. The Olsen cycle was employed to examine the thermal energy storage, and Maxwell's equations were used to determine the electrocaloric performance.

2 Experimental details

The $Ba_{0.7}Ca_{0.3}TiO_3$ composition was fabricated through a solid-state reaction route using precursors like BaO_2 (99.9%), $CaCO_3$ (99.9%), and TiO_2 (99.9%). A stoichiometric mixture of the raw materials was weighed and ball-milled in a water medium for 24 h. After that, the mixture was calcination at 1100 °C for 12 h. The phase purity of the prepared sample was examined using the X-ray

diffraction measurement (XRD) (Rigaku, Ultima IV, Cu Kα, $\lambda = 1.5418$ Å). A scanning electron microscope was used to analyze the surface morphology (EVO-18, ZEISS-Japan). The circular pellets of diameter 10 mm and thickness 1 mm were made using PVA as a binder. The pellets were sintered at 1350 °C for 12 h in the presence of air at a slow heating rate (2 °C/min). The density of the samples was calculated using Archimedes' principle and found to be 5.60 g/cm³. For collecting dielectric and ferroelectric measurements, electrodes with silver paste were painted on both sides of sintered ceramic pellet. The temperature variant dielectric measurement was carried out using an LCR meter (HIOKI IM 3570) at different frequencies starting from 100 Hz to 1Mz. The temperature and electric field-dependent polarization–electric (PE) field loops were measured using a modified Sawyer–Tower circuit-based ferroelectric hysteresis loop tracer system (Marine India Pvt. Ltd.).

3 Result and discussion

3.1 Structural and microstructural analysis

The XRD pattern of the BCT ceramic is presented in Fig. 1a. All the observed peaks suggest the formation of a perovskite crystalline structure, signifying the complete incorporation of Ca^{2+} ion into the BT lattice. For further structural analysis, Rietveld refinement of the XRD pattern has been carried out by using "FULLPROF" software and presented in Fig. 1b. The pattern is best fitted to a combined phase of a tetragonal structure with P4mm symmetry (JCPDS 81–2205) [27] and an orthorhombic structure with Amm2 symmetry (JCPDS 75–2100 [28]). For the refinement process, atomic positions and lattice parameters of $BaTiO_3$ (for both tetragonal and orthorhombic symmetry) are chosen as the reference model. The peak profile has been fitted using the Pseudo-Voight function. The 6-coefficient polynomial function has been selected to refine the background. The scale factors, instrumental parameters, cell parameters, FWHM parameters (U, V, W), Wyckoff positions, isotropic parameters, and asymmetric parameters have been refined and the occupancy of the atoms kept fixed throughout the refinement process. In Fig. 1b black solid line represents the fitted curve over the open red circles symbolizing observed data. Olive vertical lines indicate the possible Bragg positions and the blue solid line is the differential line indicating the miss matching of observed and refined values. The flat blue line is the indication of well-fitted data. The values of fitting parameters such as R-factors (R_{Bragg}, R_p, R_{wp}, R_{exp}) and goodness of fit (χ^2) are obtained from the refinement process and listed in Table 1 along with unit cell parameters. These various refined parameters reveal the existence of mixed-phase
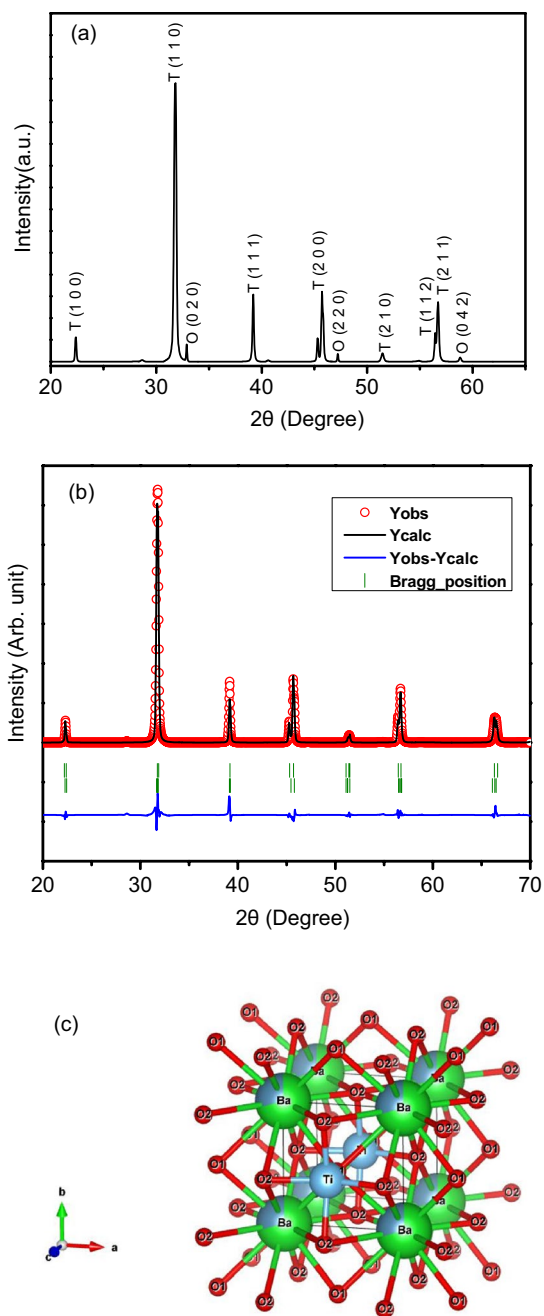
Fig. 1 **a** X-ray diffraction pattern, **b** Rietveld refinement, and **c** Unit cell structure of BCT ceramics

Table 1 Structural parameters obtained from the Rietveld refinement

Structure	Tetragonal (78.73%)	Orthorhombic (21.27%)
Space group	P4mm	Amm2
a (A^0)	3.96868	3.96232
b (A^0)	3.96868	5.63468
c (A^0)	4.00346	5.65328
Ba(x)	0	0
Ba(y)	0	0
Ba(z)	− 0.00876	0.01315
Ca(x)	0	0
Ca(y)	0	0
Ca(z)	− 0.00876	0.01315
Ti(x)	0.5	0.5
Ti(y)	0.5	0
Ti(z)	0.47712	0.57523
O(x)		
O_1	0.5	0
O_2	0.5	0.5
O(y)		
O_1	0.5	0
O_2	0	0.23380
O(z)		
O_1	0.18806	0.81077
O_2	0.58085	0.59715
R_{Bragg}	5.872	6.884
R_p	13.1	
R_{wp}	22.4	
R_{exp}	11.49	
χ^2	3.81	

of tetragonal and orthorhombic symmetry with 78.73% and 21.23%, respectively. Figure 1c shows the unit cell structure that has been obtained with the help of VESTA software. Figure 2 depicts the SEM micrographs of the $Ba_{0.7}Ca_{0.3}TiO_3$ ceramic having inhomogeneous grains size distribution. Well, dense microstructure without much porosity and co-existence of large and smaller grains was observed. The larger grains are formed due to the agglomeration of smaller grains.
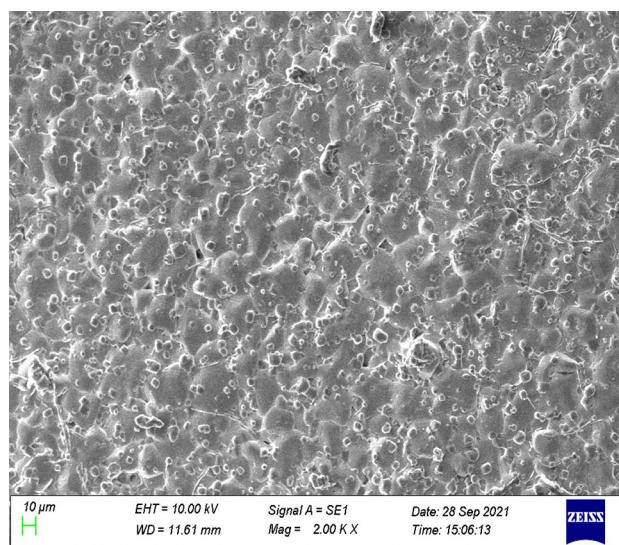

Fig. 2 Scanning electron microscopy image of BCT

3.2 Dielectric analysis

The temperature-dependent dielectric permittivity (ϵ_r) of $Ba_{0.7}Ca_{0.3}TiO_3$ ceramic at different frequencies is shown in Fig. 3a. The dielectric permittivity initially increases with temperature up to 84 °C and then reduces with an increase in temperature indicating the phase transition temperature. It is also observed that the dielectric peaks decrease with an increase in frequency. The diffuse nature of phase transitions was studied using a modified Curie–Weiss relationship as given below [29, 30].

$$\frac{1}{\epsilon_r} - \frac{1}{\epsilon_m} = \left(T - T_m\right)^{\gamma}/C_1 \tag{1}$$

where γ and C_1 were assumed to be constants. The value of γ signifies the behavior of the phase transition. When the γ value is close to 1, it shows normal ferroelectric behavior and when γ is close to 2 it shows a diffuse phase transition

behavior [29]. The plot of $\ln\left[\frac{1}{\epsilon_r} - \frac{1}{\epsilon_m}\right]$ vs $\ln[T - T_m]$ at 100 Hz is shown in Fig. 3b and the value of $\gamma = 1.69$ was obtained by fitting the experimental data according to Eq. (1). The obtained value of γ indicates a diffused phase transition in the composition that can be derived due to the presence of a polar cluster (orthorhombic phase) [31]. Further, the diffuse nature may be originated due to the development of the structural disorder in the composition [32].

3.3 Ferroelectric properties

3.3.1 Effect of electric field and temperature on the polarization

The field-dependent hysteresis loops of $Ba_{0.7}Ca_{0.3}TiO_3$ ceramic at 30 °C are presented in Fig. 4a. It is found that the maximum (P_{max}) and remnant polarization (P_r) increase as the electric field increases. The increase in polarization with an increasing electric field is because a larger electric field provides more driving force for ferroelectric domain switching [33]. The domain volume increases as the driving force increases. Consequently, an applied electric field causes an increase in the total polarization, which further increases the hysteresis parameters. A representative plot of temperature-dependent hysteresis loops at an electric field of 40 kV/cm is shown in Fig. 4b. Well-defined hysteresis loops were observed up to the transition temperature and the loop starts vanishing beyond the transition temperature. However, the P-E loops did not vanish at T_C due to the diffuse phase transition behavior. It is also found that as the temperature increases, P_s and P_r gradually decrease and this may be because the thermal agitation gradually destroys the order of arrangement of dipoles [27]. The loop becomes thinner as the temperature rises, which increases its energy storage capacity.

3.4 Pyroelectric properties

The pyroelectric coefficient was measured using the equation given below:

$$p = -\frac{dP_r}{dt} \tag{2}$$

where p, P_r, and T are the pyroelectric coefficient, remanent polarization, and temperature, respectively. Figure 5 shows the variation of pyroelectric coefficient as a function of temperature. The significant figure of merit (FOM) associated with the pyroelectric performance has been calculated using the following equations [34–36]
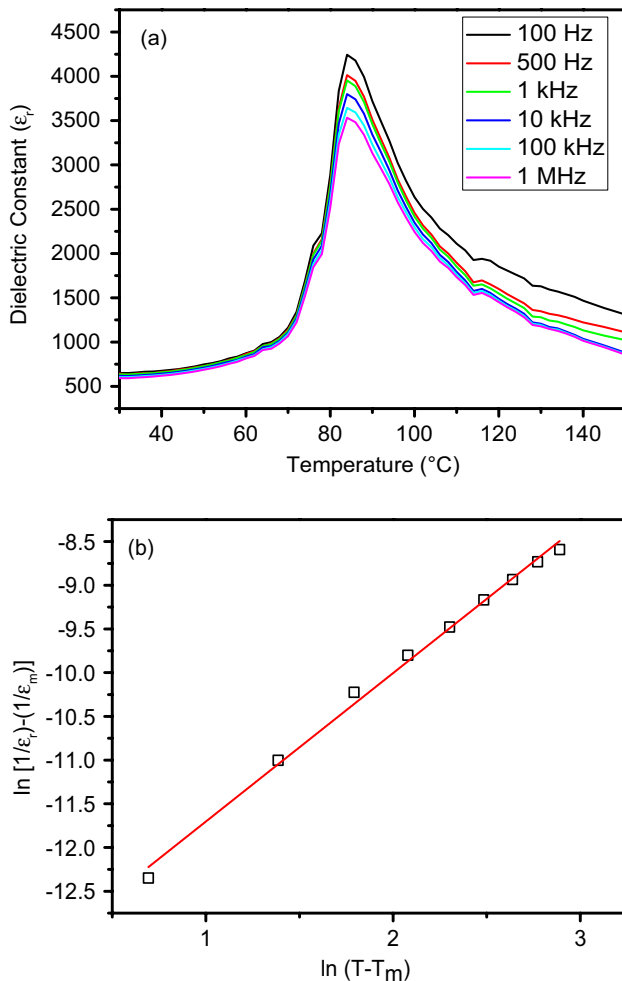
$$F_i = \frac{p}{C_V} \tag{3}$$

Fig. 3 **a** Dielectric constant as a function of temperature and **b** plot of $\ln(1/\epsilon_r - 1/\epsilon_m)$ as a function of $\ln(T - T_m)$ at 1 kHz for BCT ceramics
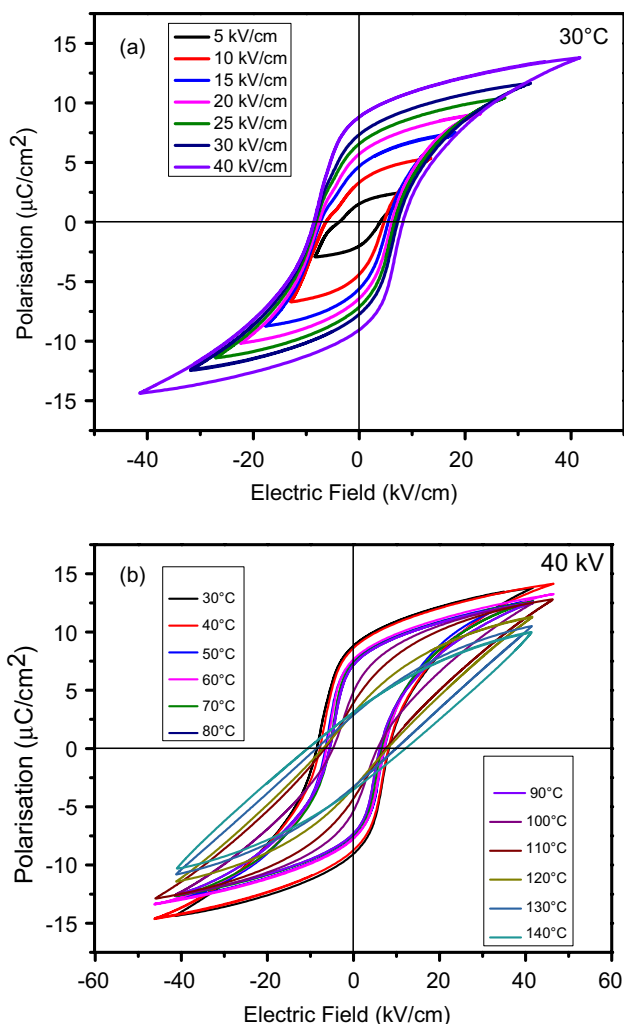
Fig. 4 P–E hysteresis loops **a** with different electric-field at temperature of 30 °C, **b** at varying temperature for an electric field of 40 kV/cm of BCT ceramics

$$F_v = \frac{p}{\varepsilon_r \varepsilon_0 C_V} \tag{4}$$

$$F_e = \frac{p^2}{\varepsilon_r \varepsilon_0} \tag{5}$$

$$F_e^* = \frac{p^2}{\varepsilon_r \varepsilon_0 C_V^2} \tag{6}$$

$$F_d = \frac{p}{C_V \sqrt{\varepsilon_r \varepsilon_0 tan\delta}} \tag{7}$$

where C_v, F_i, F_v, F_e, F_e^* and F_d are the volume-specific heat capacity which is a product of ρ density and C_p pressure-specific heat capacity taken from the literature [37],
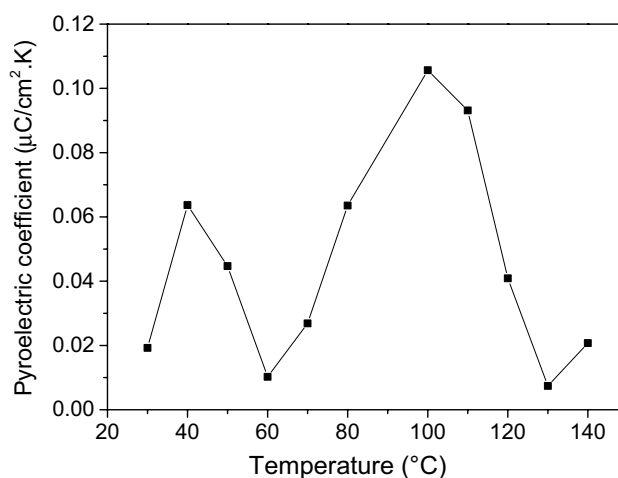

Fig. 5 Variation of Pyroelectric coefficient with temperature

the potential current responsivity performance, the voltage responsivity, pyroelectric energy harvesting figure of merit, the modified figure of merit and the detection capability, respectively. The FOMs at 373 K are found to be $F_i = 0.43 \times 10^{-1}$ m V^{-1}, $F_v = 0.2$ m^2 C^{-1}, $F_e = 5.22$ J m^{-3} K^{-2}, $F_e^* = 0.08 \times 10^{-11}$ m^3 J^{-1} and $F_d = 14.7$ Pa$^{0.5}$ for BCT ceramic.

3.5 Thermal energy storage

The hysteresis is a measure of the difference in energy, expressed as heat, needed to polarise and depolarize the ferroelectric material. Heat absorbing ability makes the material competent to generate electricity. The Olsen cycle is a reversible polarization that is meant to follow a clockwise loop between two distinct ranges of temperature and is mostly used to convert thermal energy into electricity. Two isothermal and two isoelectric field processes constitute this cycle [38]. Figure 6 represents the thermal energy conversion using the Olsen cycle. The area encompassed between A, B, C, D, and A represents the amount of electricity generated per unit volume per cycle [39]. Process A-B represents one of the two isothermal processes at a lower temperature (T_L) with an increasing low electric field limit (E_L) to a higher electric field limit (E_H) for which the corresponding polarization also increases. In the following process B-C, there is a production of lattice vibration and a rise in temperature due to the supply of heat (Q_s) to the material. Depolarization takes place while the electric field is constant, E_H, which generates a larger depolarization current that might be utilized for powering electronic equipment. The material's temperature then rises from its starting low temperature (T_L) to its final high temperature (T_H). Now, in process C-D, at constant temperature T_H the electric field is reduced
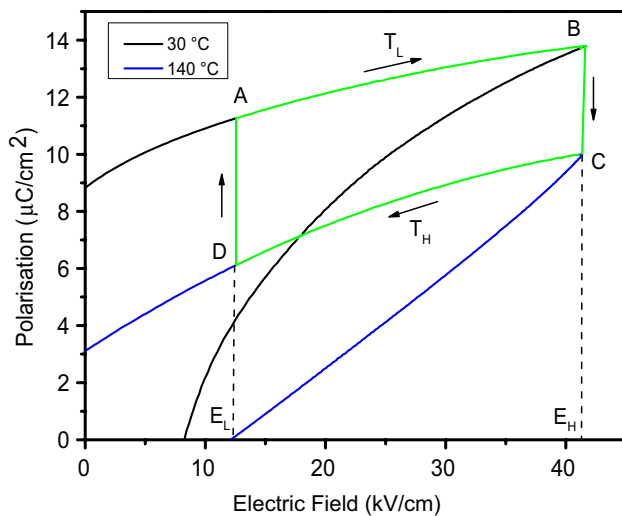
Fig. 6 Thermal energy conservation of $Ba_{0.7}Ca_{0.3}TiO_3$ ceramic using Olsen Cycle

Fig. 7 Energy storage efficiency of BCT ceramic as a function of temperature

from E_H to E_L, which generates a weak polarization current. Lastly, in process D-A, heat is extracted from the system at a constant electric field (E_L) for the material to return to its starting state and finish the cycle. Several articles provide an in-depth analysis of the Olsen cycle [39–41]. The following equation can be used to evaluate the material's isoelectric heat rejection energy density (N_D) per unit volume:

$$N_D = \oint E.dP \qquad (8)$$

where E and P denote the electric field and polarization, respectively. The Olsen cycle is used to calculate the thermal energy conversion density as shown in Fig. 6. A maximum thermal energy conversion density of 132 kJ/cm^3 is obtained per cycle for the present composition which is comparable with the energy conversion density of 150 kJ/m^3 per cycle for PZN-5.5PT based on the pyroelectric effect [42].

A temperature-dependent P-E hysteresis loop can be used to determine a dielectric material's ability to store electrical energy. The recoverable energy density (W_{rec}) and total energy density (W_{tot}) can be evaluated by integrating the region between the polarization axis and the upper and lower branches of the P-E hysteresis loop, respectively. The following equations are used to find the W_{rec}, W_{tot}, and energy storage efficiency η [43].
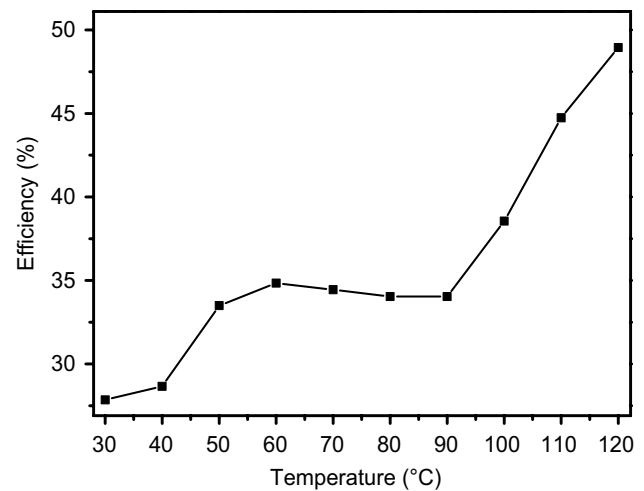
$$w_{tot} = \int_{0}^{P_{max}} EdP \qquad (9)$$

$$w_{rec} = \int_{P_r}^{P_{max}} EdP \qquad (10)$$

$$\eta = \frac{W_{rec}}{W_{tot}} X100 = \frac{W_{rec}}{W_{rec} + W_{loss}} X100 \qquad (11)$$

Figure 7 represents the trend of energy efficiency of BCT ceramics as a function of temperature. In the present work, the maximum values of W_{rec} and W_{tot} are found to be 177.5 mJ/cm^3 and 79.6 mJ/cm^3 at 100 °C, respectively, with an energy storage efficiency of 46% for 40 kV/cm. Additionally, energy storage efficiency rises with temperatures up to 120 °C, reaching a maximum of 49%.

Besides the high energy density, another factor that is crucial for practical application is thermal stability, which is given by the following equation [44].

$$\frac{\Delta W_{rec,T}}{W_{rec,300K}} = \left| \frac{W_{rec,T} - W_{rec,300K}}{W_{rec,300K}} \right| \qquad (12)$$

where $W_{rec,T}$ is the value of W_{rec} at temperature T and $\Delta W_{rec,T}$ is the difference between $W_{rec,T}$ and $W_{rec,300K}$. The thermal stability is found to be 6.59% in a temperature range of 40–110 °C which is an indication of good thermal stability in the composition.

3.6 Electrocaloric properties

The electrocaloric effect has been studied for the $Ba_{0.7}Ca_{0.3}TiO_3$ ceramic using an indirect method. For this
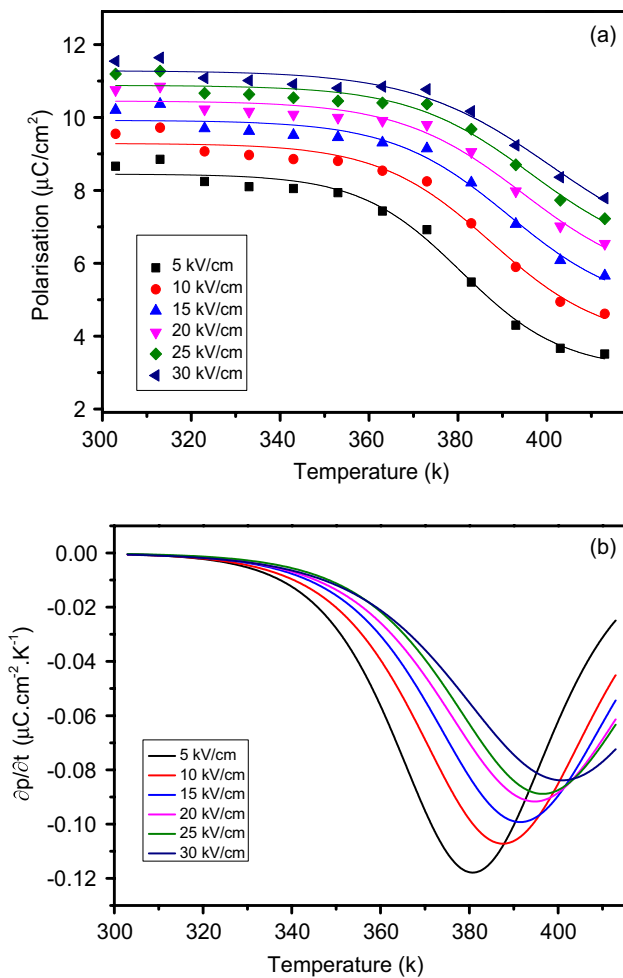
Fig. 8 Plot for **a** temperature-dependent polarization at different electric fields, **b** pyroelectric response $\left(\frac{\partial P}{\partial T}\right)_E$ at different electric fields for BCT ceramics
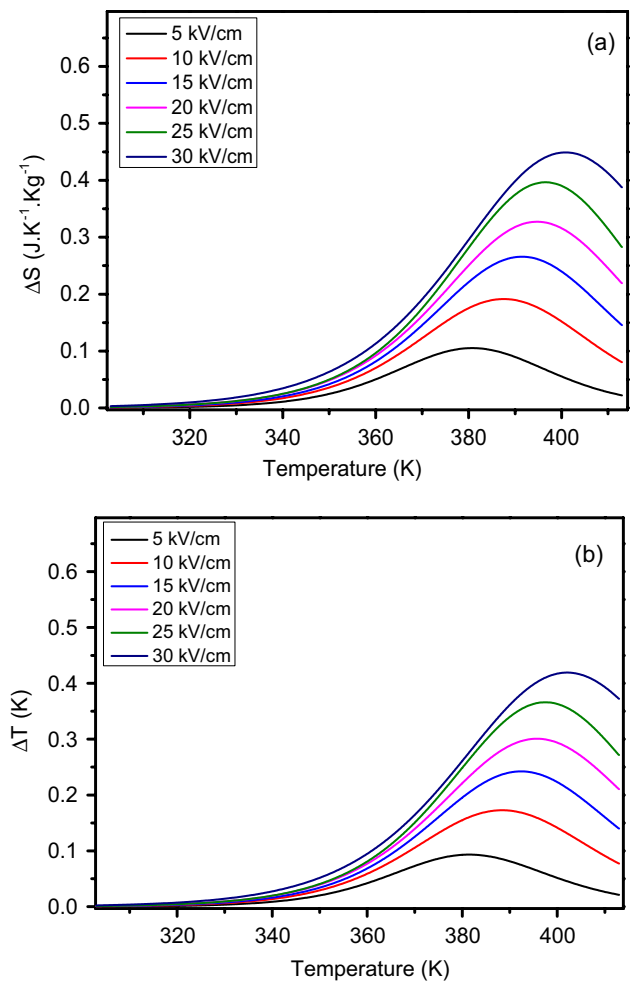

Fig. 9 Temperature dependent **a** entropy change (ΔS) and **b** adiabatic temperature change (ΔT) at different electric fields for BCT ceramics

method, a graph is plotted between polarization vs temperature for an increasing electric field. Considering the upper branches of the temperature-dependent P-E loop, the polarization values for various electric fields were determined. Boltzmann non-linear curve fitting is used to obtain the polarization versus temperature (P–T) curve as shown in Fig. 8a. It is observed that the polarization increases with an increase in the electric field. Also, as the temperature increases, saturation polarization decreases accordingly to Curie–Weiss Law [45].

Now assuming the Maxwell relation $\left(\frac{\partial P}{\partial T}\right)_E = \left(\frac{\partial S}{\partial E}\right)_T$, the isothermal temperature change (ΔT) and adiabatic entropy change (ΔS) can be calculated to study the EC behavior, using the following equation [46].

$$\Delta T = -\frac{1}{\rho} \int_{E_1}^{E_2} \frac{T}{C_p} \left(\frac{\partial P}{\partial T}\right) dE \tag{13}$$

$$\Delta S = -\frac{1}{\rho} \int_{E_1}^{E_2} \left(\frac{\partial P}{\partial T}\right) dE \tag{14}$$

where (ρ) is the density of BCT ceramics found to be 5.60 g/cm^3 by Archimedes method. (C_p) is the specific heat capacity which is 434 J.kg^{-1} K^{-1} obtained from the literature [46]. E_2 is the final applied electric field and E_1 is the lowest electric field which is set to zero.

Figure 8b represents the pyroelectric response $\left(\frac{\partial P}{\partial T}\right)_E$ as a function of temperature at different electric fields. It is seen from the graph that the appearance of peaks for an electric field may contribute to the ferroelectric to paraelectric phase change [47]. Figure 9a, b denotes the
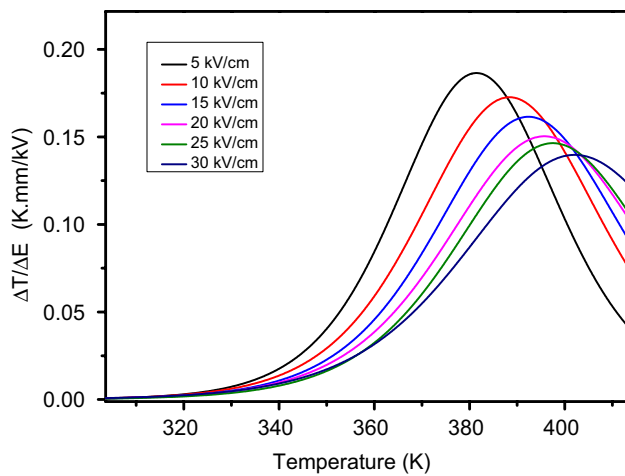
Fig. 10 The temperature dependence of the electrocaloric strength ΔT/ΔE at different electric fields

temperature-dependent ΔT and ΔS under different electric fields, respectively. It is observed that ΔT and ΔS increases with an increase in electric fields. The maximum ΔS (0.44 J/K. kg) is obtained at an applied electric field of 30 kV/cm at around 400 K. Similarly, a maximum ΔT of 0.419 K is observed at an applied field of 30 kV/cm. The EC field strength (ξ) can be calculated for maximum ΔT per change in the applied field, i.e., ($\Delta T/\Delta E$) and is found to be 0.013 K.cm/kV [48]. Figure 10 shows the temperature dependence of the electrocaloric strength $\Delta T/\Delta E$ at different electric fields of $Ba_{0.7}Ca_{0.3}TiO_3$ ceramic. Also, a material possessing high saturation electric field E can be expected to have high adiabatic temperature change as high energy is needed for back-switching. So, there can be two ways to improve the ECE of ferroelectric ceramics, i.e., either by raising the electric field's strength or the polarization gradient [49]. An essential factor for figuring out the effectiveness of the material and estimating the performance of the refrigeration cycle is the coefficient of performance (COP), which is obtained by the following equation [50].

$$COP = \left| \frac{Q}{W_{rec}} \right| = \frac{|\Delta SXT|}{|W_{rec}|} \tag{15}$$

where Q and W_{rec} are the isothermal heat and recovered density. In our work the COP of BCT ceramics is found to be 5.69 at around 393 K. Good COP value indicates good cooling performance, indicating BCT with a considerable amount of ΔT, ΔS, and COP has the potential for future application in electrocaloric solid-state cooling devices.

4 Conclusion

The traditional solid-state reaction technique was used to synthesize the BCT ceramic. XRD revealed the development of the phase structure, and Rietveld refinement verified it. Images from the SEM showed a rich microstructure. The dielectric performance as a function of temperature showed a diffuse phase transition. The temperature dependence of ferroelectric characteristics at different fields revealed that polarization increases with field and decreases with temperature. The pyroelectric coefficient and the figure of merits (FOMs) for detectivity (F_d), energy harvesting (F_e and F_e^*), voltage responsivity (F_v), and current responsivity (F_i) were also estimated. The results indicated that the ceramic might be a great candidate for pyroelectric device. Under operating conditions of 30 °C to 140 °C and an electric field of 0 to 3 MV/m, the highest thermal energy densities of 132 kJ/cm³ per cycle were noted. Additionally, the Maxwell relation was used as an indirect way to obtain increased electrocaloric values as isothermal entropy change $\Delta S = 0.44$ J/K. Kg, adiabatic temperature change $\Delta T = 0.419$ K, electrocaloric strength $\Delta T/\Delta E = 0.013$ K.cm/kV, and COP = 5.69 in BCT ceramic. As a result, the environmentally friendly BCT ceramic performance is improved, making it a suitable choice for solid-state electrocaloric cooling and energy storage density capacitors.

Data availability Data will be available on reasonable request.

Declarations

Conflict of interest On behalf of all authors, the corresponding author states that there is no conflict of interest.

References

1. A.K. Sagotra, D. Errandonea, C. Cazorla, Nat. Commun. **8**, 963 (2017)
2. X. Moya, S. Kar-Narayan, N.D. Mathur, Nat. Mater. **13**, 5 (2014)
3. X. Moya, E. Defay, V. Heine, N.D. Mathur, Nat. Phys. **11**, 3 (2015)
4. L. Manosa, A. Planes, M. Acet, J. Mater. Chem. A **1**, 4925–4936 (2013)
5. M. Valant, Prog. Mater. Sci. **57**(6), 980–1009 (2012)
6. V. Franco, J.S. Blazquez, J.J. Ipus, J.Y. Law, L.M. Moreno-Ramírez, A. Conde, Prog. Mater. Sci. **93**, 112–232 (2018)
7. L. Mañosa, A. Planes, Adv. Mater. **29**, 1603607 (2017)

8. Y. Liu, G. Zhang, Q. Li, L. Bellaiche, J.F. Scott, B. Dkhil, Q. Wang, Phys. Rev. B **94**, 214113 (2016)

9. B. Li, Y. Kawakita, S. Ohira-Kawamura, T. Sugahara, H. Wang, J. Wang, Y. Chen, S.I. Kawaguchi, S. Kawaguchi, K. Ohara, K. Li, D. Yu, R. Mole, T. Hattori, T. Kikuchi, S.I. Yano, Z. Zhang, Z. Zhang, W. Ren, S. Lin, O. Sakata, K. Nakajima, Z. Zhang, Colossal Nat. **567**(7749), 506–510 (2019)

10. J. Shi, D. Han, Z. Li, L. Yang, S.G. Lu, Z. Zhong, J. Chen, Q.M. Zhang, X. Qian, Joule **3**(5), 1200–1225 (2019)

11. R. Ma, Z. Zhang, K. Tong, D. Huber, R. Kornbluh, Y.S. Ju, Q. Pei, Science **357**(6356), 1130–1134 (2017)

12. D. Fu, M. Itoh, in *Ferroelectric Materials-Synthesis and Characterization*, ed. by A. Peláiz-Barranco (Intech open, London, 2015), p. 105

13. H. Kacem, Z. Sassi, M.A. Gdaiem, A. Dhahri, L. Seveyrat, L. Lebrun, J. Dhahri, Inorg. Chem. Commun. **144**, 109771 (2022)

14. H. Kacem, A. Dhahri, M.A. Gdaiem, Z. Sassi, L. Seveyrat, L. Lebrun, J. Dhahri, Appl. Phys. A Mater. Sci. Process. **127**(6), 1–10 (2021)

15. G. Liu, Y. Li, M. Shi, L. Yu, P. Chen, K. Yu, J. Gao, Ceram. Int. **45**(15), 19189–19196 (2019)

16 Y.H. Huang, J.J. Wang, T.N. Yang, Y.J. Wu, X.M. Chen, L.Q. Chen, Appl. Phys. Lett. **112**(10), 102901 (2018)

17. W. Liu, X. Ren, Phys. Rev. Lett. **103**(25), 257602 (2009)

18. Y. Yao, C. Zhou, D. Lv, D. Wang, H. Wu, Y. Yang, X. Ren, EPL **98**(2), 27008 (2012)

19. C.-X. Li, B. Yang, S.-T. Zhang, R. Zhang, W.-W. Cao, Ceram. Inter. **39**, 2967–2973 (2013)

20. V.S. Puli, D.K. Pradhan, B.C. Riggs, D.B. Chrisey, R.S. Katiyar, J. Alloy. Compd. **584**, 369–373 (2014)

21. P. Jaiban, N. Pisitpipathsin, P. Wannasut, A. Watcharapasorn, Ferroelectr. **533**, 165–172 (2018)

22. P. Wannasut, N. Pisitpipathsin, A. Watcharapasorn, P. Jaiban, C. Mai, J. Sci. **45**(7), 2817–2825 (2018)

23. G.P. Cao, H.B. Huang, D.S. Liang, X.Q. Ma, Ceram. Inter. **43**(9), 6671–6676 (2017)

24. P. Sharma, P. Kumar, R.S. Kundu, J.K. Juneja, N. Ahlawat, R. Punia. Ceram. Inter. **41**, 13425–13432 (2015)

25. S. Patel, L. Kodumudi Venkataraman, H. Yadav, J. Korean Ceram. Soc. **58**, 337–350 (2021)

26. P.S. Kadhane, B.G. Baraskar, T.C. Darvade et al., J. Korean Ceram. Soc. **59**, 578–588 (2022)

27. Y. Bai, F. Han, S. Xie, J. Li, S. Qin, J. Li, L. Qiao, D. Guo, J. Alloys Compd. **736**, 57–61 (2018)

28. P. Ge, X. Tang, Q. Liu, Y. Jiang, W. Li, J. Luo, J. Mater. Sci. Mater Electron. **29**, 1075–1081 (2018)

29. S.N. Uchino, Ferroelectr. Lett. Sect. **44**, 55–61 (1982)

30. D. Viehland, M. Wuttig, L.E. Cross, Ferroelectrics **120**, 71–77 (1991)

31. T. Maiti, R. Guo, A.S. Bhalla, J. Am. Ceram. Soc. **91**(6), 1769–1780 (2008)

32 X. Liu, F. Li, P. Li, J. Zhai, B. Liu, J. Eur. Ceram. Soc. **37**, 4585 (2017)

33. N. Wongdamnern, N. Triamnak, M. Unruan, K. Kanchiang, A. Ngamjarurojana, S. Ananta, R. Yimnirun, Phys. Lett. A **374**(3), 391–395 (2010)

34. W.L. Zhang, Y.C. Yu, W.B. Luo, Y. Shuai, X.Q. Pan, Q.Q. Wu, C.G. Wu, Infrared Phys. Technol. **80**, 100–104 (2017)

35. P. Yu, Y. Ji, N. Neumann, S.G. Lee, H. Luo, M. Es-Souni, IEEE Trans. Ultrason. Eng. **59**(9), 1983–1989 (2012)

36. C.R. Bowen, J. Taylor, E. LeBoulbar, D. Zabek, A. Chauhan, R. Vaish, Energy Environ. Sci. **7**(12), 3836–3856 (2014)

37. Yi. He, Thermochim. Acta **419**, 135–141 (2004)

38. R. Olsen, D. Bruno, Pyroelectric Convers. Mater. IECEC' **86**, 89–93 (1986)

39. A. Chauhan, S. Patel, G. Vats, R. Vaish, Energy Technol. **2**, 205–209 (2014)

40. C. Bowen, J. Taylor, E. Le Boulbar, D. Zabek, A. Chauhan, R. Vaish, Energy Environ. Sci. **7**, 3836–3856 (2014)

41. F.Y. Lee, S. Goljahi, I.M. McKinley, C.S. Lynch, L. Pilon, Smart Mater. Struct. **21**, 025021 (2012)

42. I.M. McKinley, R. Kandilian, L. Pilon, Smart Mater. Struct. **21**, 035015 (2012)

43. S. Khardazi, H. Zaitouni, S. Belkhadir, D. Mezzane, M. Amjoud, Y. Gagou, B. Asbani, I. Lukyanchuk, S. Terenchuk, J. Solid State Chem. **311**, 123112 (2022)

44. P. Butnoi, S. Manotham, P. Jaita, C. Randorn, G. Rujijanagul, J. Eur. Ceram. Soc. **38**(11), 3822–3832 (2018)

45. S. Patel, A. Chauhan, R. Vaish, Int. J. Appl. Ceram. Technol. **12**, 899–907 (2015)

46 A. Bauza, T.J. Mooibroek, A. Frontera et al., Cryst. Eng. Comm. **18**(1), 10–23 (2016)

47. B.B. Liu, X.H. Wang, R.X. Zhang, L.T. Li, J. Am. Ceram. Soc. **100**, 3599–3607 (2017)

48. M. Sanlialp, V.V. Shvartsman, M. Acosta, D.C. Lupascu, J. Am. Ceram. Soc. **99**, 4022–4030 (2016)

49. Z. Luo, D. Zhang, Y. Liu, D. Zhou, Y. Yao, C. Liu, B. Dkhil, X. Ren, X. Lou, Appl. Phys. Lett. **105**, 102904 (2014)

50. E. Defay, S. Crossley, S. Kar-Narayan, X. Moya, N.D. Mathur, Adv. Mater. **25**(24), 3337–3342 (2013)